

The Nanoscale Structure and Stability of Organic Photovoltaic Blends Processed with Solvent Additives

Rachel C. Kilbride,* Emma L. K. Spooner, Stephanie L. Burg, Bárbara L. Oliveira, Ana Charas, Gabriel Bernardo, Robert Dalgliesh, Stephen King, David G. Lidzey, Richard A. L. Jones, and Andrew J. Parnell*

Controlling the nanomorphology in bulk heterojunction photoactive blends is crucial for optimizing the performance and stability of organic photovoltaic (OPV) technologies. A promising approach is to alter the drying dynamics and consequently, the nanostructure of the blend film using solvent additives such as 1,8-diiodooctane (DIO). Although this approach is demonstrated extensively for OPV systems incorporating fullerene-based acceptors, it is unclear how solvent additive processing influences the morphology and stability of nonfullerene acceptor (NFA) systems. Here, small angle neutron scattering (SANS) is used to probe the nanomorphology of two model OPV systems processed with DIO: a fullerene-based system (PBDB-T:PC₇₁BM) and an NFA-based system (PBDB-T:ITIC). To overcome the low intrinsic neutron scattering length density contrast in polymer:NFA blend films, the synthesis of a deuterated NFA analog (ITIC-d₅₂) is reported. Using SANS, new insights into the nanoscale evolution of fullerene and NFA-based systems are provided by characterizing films immediately after fabrication, after thermal annealing, and after aging for 1 year. It is found that DIO processing influences fullerene and NFA-based systems differently with NFA-based systems characterized by more phase-separated domains. After long-term aging, SANS reveals both systems demonstrate some level of thermodynamic induced domain coarsening.

1. Introduction

Organic photovoltaic (OPV) bulk heterojunction blends comprising donor polymers and small molecule acceptors (SMA) show promise for a range of low cost, light weight, and flexible applications (e.g. portable electronics).^[1,2] The commercial success of these technologies relies on the fabrication of devices that are both efficient and stable. The emergence of nonfullerene acceptors (NFAs) has enhanced power conversion efficiencies (PCEs) beyond 19%,^[3] due to their superior optoelectronic properties compared to traditional fullerene-based acceptors.^[4–8] However, the stability of OPVs falls short of the proposed > 20 year real-world lifetimes required for commercialization, necessitating efforts to identify key degradation routes and strategies to mitigate performance loss.^[9]

A critical parameter in the light-harvesting process for OPV devices is the exciton diffusion length (l_d) which defines

R. C. Kilbride
Department of Chemistry
The University of Sheffield
Dainton Building, Brook Hill, Sheffield S3 7HF, United Kingdom
E-mail: r.c.kilbride@sheffield.ac.uk

R. C. Kilbride, E. L. K. Spooner, S. L. Burg, D. G. Lidzey, A. J. Parnell
Department of Physics and Astronomy
The University of Sheffield
Hicks Building, Hounsfield Road, Sheffield S3 7RH, United Kingdom
E-mail: a.j.parnell@sheffield.ac.uk

E. L. K. Spooner
The Photon Science Institute
The University of Manchester
Oxford Road, Manchester M13 9PY, United Kingdom

B. L. Oliveira, A. Charas
Instituto de Telecomunicações
Instituto Superior Técnico
Av. Rovisco Pais, Lisboa P-1049-001, Portugal

G. Bernardo
LEPABE – Laboratory for Process Engineering
Environment
Biotechnology and Energy
Faculty of Engineering
University of Porto
Porto 4200–465, Portugal

G. Bernardo
ALiCE – Associate Laboratory in Chemical Engineering
Faculty of Engineering
University of Porto
Porto 4200–465, Portugal

R. Dalgliesh, S. King
ISIS Neutron and Muon Spallation Source
Rutherford Appleton Laboratories
Oxfordshire OX11 0QX, United Kingdom

R. A. L. Jones
Department of Materials
The University of Manchester
Sackville Street Building, Manchester M1 3BB, United Kingdom

 The ORCID identification number(s) for the author(s) of this article can be found under <https://doi.org/10.1002/smll.202311109>

© 2024 The Authors. Small published by Wiley-VCH GmbH. This is an open access article under the terms of the [Creative Commons Attribution License](https://creativecommons.org/licenses/by/4.0/), which permits use, distribution and reproduction in any medium, provided the original work is properly cited.

DOI: 10.1002/smll.202311109

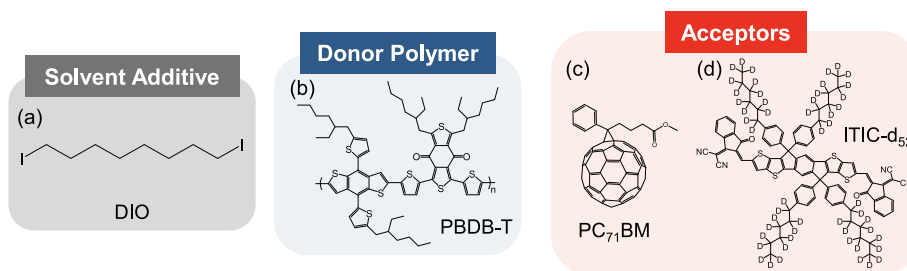


Figure 1. Chemical structures of a) solvent additive, 1,8-diiodooctane (DIO), b) donor polymer, PBDB-T, c) fullerene acceptor, PC₇₁BM, and d) deuterated non-fullerene acceptor, ITIC-d₅₂.

the average distance over which an exciton exists before recombination (typically ≈ 10 – 50 nm).^[10,11] The highest efficiency OPV devices comprise a phase-separated blend film characterized by length scales comparable to l_d , to provide optimal polymer:SMA heterointerfaces for efficient exciton dissociation. Due to the asymmetry in the molecular size of polymer and SMA components, polymer:SMA blends typically form a metastable pure SMA phase, and a mixed, majority polymer phase.^[12,13] Over time the blend morphology can evolve due to kinetic and thermodynamic driving factors. The thermodynamic equilibrium depends on polymer:SMA miscibility, typically measured using the Flory-Huggins interaction parameter (χ). High χ values indicate poor miscibility and phase separation is thermodynamically favorable. In contrast, kinetic equilibrium is influenced by the diffusion coefficients of the components, which is strongly related to the glass transition temperature.^[14] Low diffusion coefficients, and kinetic hindrance, can stabilize a system, even when phase separation is thermodynamically favorable.^[13] This balance between kinetic and thermodynamic factors drives morphological changes over time.

Many processing routes have been explored to optimize blend nanomorphology, such as thermal annealing, solvent annealing, and solvent additives.^[15–18] The latter involves the addition of a small volume of a high boiling point solvent additive to the processing solvent to prolong film drying and tune the solubility of the polymer/SMA components.^[19,20] The most promising additives include alkanedithiols and di(X)octanes, where X is a small, polarizable functional group such as a halogen.^[21–23] The most widely used of these is 1,8-diiodooctane (DIO, **Figure 1a**), which has been shown to impact the performance and stability of fullerene and NFA-based devices differently with NFA systems often optimized at much smaller concentrations.^[24,25] Additionally, DIO has demonstrated contrasting effects on the morphology of freshly prepared blend films and blend films that have been aged over time, with reports of both an increase and a decrease in domain size.^[20,25–28] Furthermore, DIO is known to induce catastrophic UV-initiated radical reactions, even in trace amounts, for both fullerene and nonfullerene acceptors, impacting the long-term stability of devices.^[29–31] It has also been implicated in reactions with acidic PEDOT:PSS, and changes in vertical segregation of BHJ components.^[32–34] Moreover, it can be difficult to fully remove DIO from a BHJ film after deposition,^[29] meaning that such effects may be difficult to avoid, and the long-term morphological impact during operational timescales has yet to be established. Understanding the differences in DIO processing between fullerene and NFA-based systems, alongside dif-

ferences in associated instability, remains a key area of exploration.

Various techniques such as atomic force microscopy (AFM), electron microscopy, X-ray scattering have been used to establish a correlation between film morphology and device performance.^[35] However, electron microscopy and X-ray scattering are often limited by the inherent poor contrast between the carbon-based polymer and SMA, leading to ambiguity in the interpretation of these results. Furthermore, microscopy techniques such as AFM only provide information from a small area of the film surface, which may not be representative of the bulk morphology.

In this work, small angle neutron scattering (SANS) was used to investigate the impact of DIO on the nanostructure evolution of an archetypal polymer: NFA system and a comparative polymer:fullerene system. SANS is an established structural characterization technique that probes the average bulk nanostructure of a system in the length scale range ≈ 1 – 100 nm (see Note S1, Supporting Information:SANS). The highly penetrative and nondestructive nature of neutrons makes them an ideal probe to study organic systems that contain light atoms such as hydrogen and carbon. For fullerene-based systems, the high intrinsic scattering length density (SLD) of the fullerene acceptor typically leads to substantial neutron SLD contrast with the polymer or solvent, and the systems can be studied without deuteration both in the solid-state,^[26,28,36–40] and solution-state.^[41,42]

The model systems of choice in this study were blends of the donor polymer poly[(2,6-(4,8-bis(5-(2-ethylhexyl)thiophen-2-yl)-benzo[1,2-b:4,5-b']dithiophene))-alt-(5,5-(1',3'-di-2-thienyl-5',7'-bis(2-ethylhexyl)benzo[1',2'-c:4',5'-c']dithiophene-4,8-dione)] (PBDB-T, **Figure 1b**) with a surface-functionalized fullerene [6,6]-Phenyl-C₇₁-butyric acid methyl ester (PC₇₁BM, **Figure 1c**) or NFA 3,9-bis(2-methylene-(3-(1,1-dicyanomethylene)-indanone))-5,5,11,11-tetrakis(4-hexylphenyl)-dithieno[2,3-d':2',3'-d'']-s-indaceno[1,2-b:5,6-b']dithiophene (ITIC). Due to similar chemical compositions of typical NFAs and donor polymers, the neutron SLD contrast is often insufficient for SANS measurements. Full or partial deuteration of one component can increase the neutron SLD contrast between the polymer and NFA domains resulting in a significant enhancement of the SANS intensity.^[43,44] To ensure sufficient SLD contrast with PBDB-T, we report the synthesis of a partially deuterated ITIC analog (ITIC-d₅₂, **Figure 1d**), demonstrating the first approach to characterize polymer:NFA blend films with SANS using deuterated NFAs (d-NFAs). SANS measurements reveal that DIO processing influences fullerene and NFA-based systems differently, demonstrating that the same

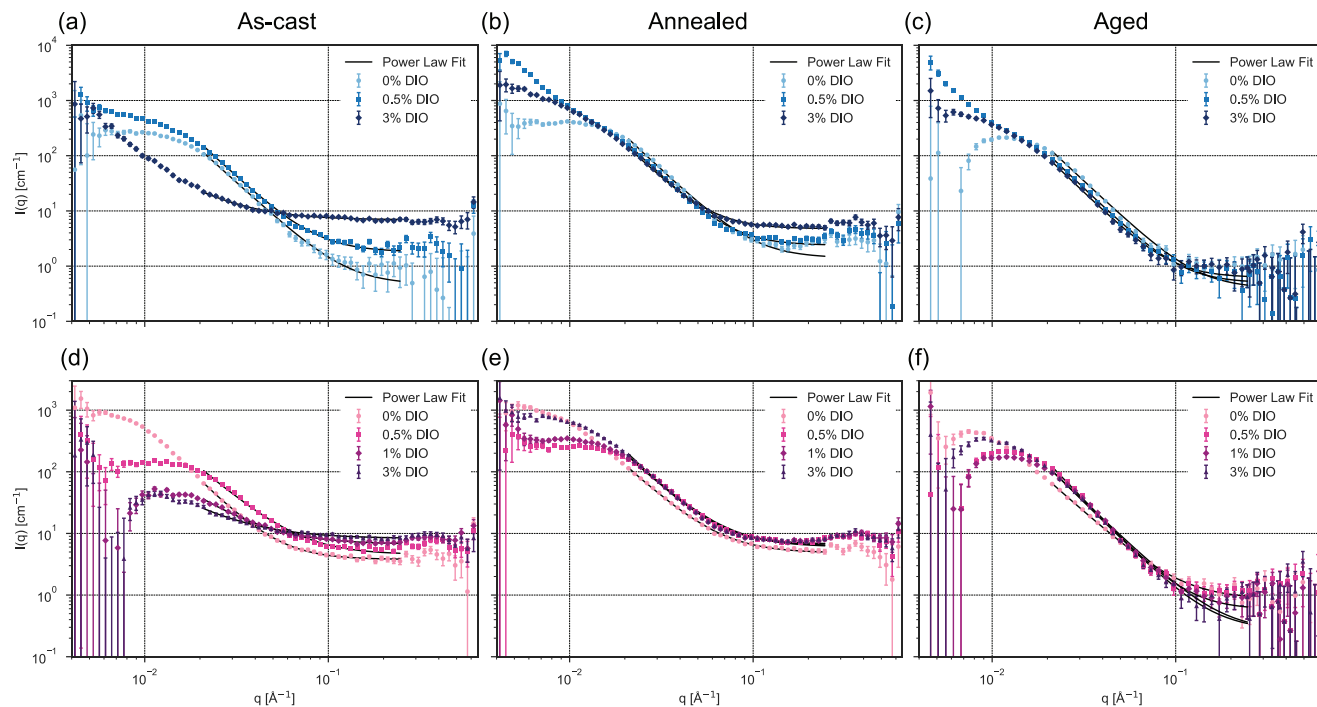


Figure 2. Absolute SANS intensity across the full observable q range of as-cast, annealed, and aged a–c) PBDB-T:ITIC- d_{52} and d–f) PBDB-T:PC $_{71}$ BM blend films processed with 0–3 vol% DIO. The power law model fits in the Porod scattering regime ($0.02 \text{ \AA}^{-1} < q < 0.25 \text{ \AA}^{-1}$) at high q are also included.

processing methods traditionally used to optimize fullerene-based systems are not easily translated to NFA-based systems. Furthermore, we demonstrate that SANS is capable of probing subtle changes in morphology after prolonged aging, making it a promising technique for further morphological stability studies.

2. Results and Discussion

The synthetic route to prepare the deuterated ITIC analog with deuterated aliphatic C6 side-chains is described in the Supporting Information (Note S2, Supporting Information: ITIC- d_{52} Synthesis and Characterization). Deuterium substitution was confirmed by ^{13}C and ^1H and NMR characterization (Figure S2 and S3, Supporting Information). A summary of the estimated SLDs for all blend materials and solvents is presented in Table S1 (Supporting Information). Compared with the hydrogenated ITIC analog, the neutron SLD contrast in the blend with PBDB-T increases by a factor of ≈ 20 when substituted with ITIC- d_{52} . The PBDB-T:ITIC- d_{52} and PBDB-T:PC $_{71}$ BM blend films were prepared on PEDOT:PSS coated quartz by spin-coating solutions of the dissolved material in chlorobenzene with various DIO concentrations ranging from 0–3 vol% DIO. Due to the limited synthetic yield of ITIC- d_{52} , PBDB-T:ITIC- d_{52} blend films were processed with DIO volume concentrations of 0, 0.5, and 3 vol%. In contrast, PBDB-T:PC $_{71}$ BM blend films were processed with DIO volume concentrations of 0, 0.5, 1, and 3 vol% (denoted 0, 0.5, 1, and 3% DIO henceforth).

The same blend films were measured as prepared, after thermal annealing at $160 \text{ }^\circ\text{C}$ for 10 min in air and again after storage in the dark under ambient conditions for 1 year (referred to as as-cast, annealed, and aged respectively). Here, we acknowl-

edge that the as-cast films are expected to be solvent-rich and the presence of solvents and their distribution within the blend films may affect the as-cast scattering results. The thermal annealing procedures used in this work replicate those used to fabricate high-efficiency PBDB-T:ITIC devices reported elsewhere.^[5] Films were aged in the dark to eliminate UV-induced radical reactions so that changes in the SANS data can be predominantly attributed to morphology changes over time. To guarantee sufficient SANS intensity, this work follows established SANS protocols, using a stack of device-relevant-thick films.^[26,28,36–38,45] This previously reported approach allows a large sample volume to be probed ($\approx 1 \times 10^8 \text{ } \mu\text{m}^3$) while ensuring that the films are representative of the bulk nanomorphology in OPV devices (i.e. the same spin-coating conditions and so the same film drying conditions), encompassing sample-to-sample variations as well as film inhomogeneities.^[26,46] To ensure scattering intensity is dominated by the bulk film and not from surface roughness effects, we performed atomic force microscopy (AFM) measurements of aged samples which shows all blend films are relatively smooth with surface roughness values in the range $\approx 1\text{--}4 \text{ nm}$ (Figure S4 and Table S2, Supporting Information). Power spectral density (PSD) analysis of the AFM data possess no systematic variation and do not match the observed SANS profiles, confirming that the observed SANS intensity originates from length scales in the blend films and not due to surface roughness effects (Figure S5, Supporting Information).

The absolute SANS intensities of all blend film samples are presented in Figure 2. In the high scattering vector (q) regime, a weak intensity peak is observed in annealed samples at $q \approx 0.3\text{--}0.35 \text{ \AA}^{-1}$, corresponding to a d -spacing ($d = 2\pi/q$) of $18\text{--}21 \text{ \AA}$. This is consistent with the PBDB-T lamellae d_{100} spacing

Table 1. The scattering exponent α obtained by fitting a power law model to the Porod scattering regime ($0.02 \text{ \AA}^{-1} < q < 0.25 \text{ \AA}^{-1}$) in Figure 2.

	PBDB-T:ITIC-d ₅₂ α			PBDB-T:PC ₇₁ BM α			
	0% DIO	0.5% DIO	3% DIO	0% DIO	0.5% DIO	1% DIO	3% DIO
As-cast	3.02 ± 0.03	3.02 ± 0.02	1.96 ± 0.10	2.90 ± 0.04	2.49 ± 0.02	1.98 ± 0.05	1.77 ± 0.08
Annealed	3.06 ± 0.01	3.14 ± 0.02	3.10 ± 0.02	2.64 ± 0.02	2.62 ± 0.01	2.73 ± 0.02	2.87 ± 0.02
Aged	3.12 ± 0.03	3.20 ± 0.04	3.22 ± 0.05	2.66 ± 0.05	3.12 ± 0.03	2.82 ± 0.03	2.95 ± 0.03

suggesting the formation of PBDB-T aggregates after annealing.^[47,48] We also note that ITIC crystallites are expected to exhibit a peak in the q range $0.30\text{--}0.35 \text{ \AA}^{-1}$ and the scattering peak in PBDB-T:ITIC-d₅₂ samples is likely a superposition of scattering from both ITIC-d₅₂ and PBDB-T crystallites.^[49] The absence of scattering in the q range $\approx 0.30\text{--}0.35 \text{ \AA}^{-1}$ after aging suggests a loss in molecular order for all samples.

2.1. Scattering Exponents in the Porod Regime

Scattering in the Porod regime ($0.02 \text{ \AA}^{-1} < q < 0.25 \text{ \AA}^{-1}$) indicates the presence of an interface. In Figure 2, all Porod regimes are fitted using a simple Power Law model $I(q) \propto q^{-\alpha}$ where α , termed the scattering exponent characterizes the diffuseness of the interface (summarized in Table 1).^[50] More specifically, α is related to the surface fractal dimension of the interface D_s ($\alpha = 6 - D_s$) where $\alpha = 2$ for mass fractals and $3 < \alpha < 4$ for surface fractals depending on the degree of surface roughness.^[51] For a smooth, sharp, 2D interface a value of $\alpha = 4$ is expected (e.g., for a highly phase-separated system). A decrease in α corresponds to an increase in D_s and is indicative of a rougher, broader interface (e.g., due to domain intermixing). Domain intermixing can lead to excessive recombination, whilst domains that are too pure have decreased interfacial area and charge percolation pathways for efficient exciton dissociation and charge extraction.^[52] Regardless of acceptor or DIO concentration, all films measured in this study exhibit $\alpha < 4$, indicative of interfacial mixing or roughening. This has also been demonstrated for PffBT4T-2OD:PC₇₁BM and P3HT:PC₆₁BM OPV systems, highlighting the complexity of OPV blend morphologies compared to the idealized two-phase system with sharp domain boundaries.^[28,38,39,51]

It is expected that all as-cast films will be solvent-rich due to residual chlorobenzene and DIO in the film after spin-coating.^[29,53] The amount of residual DIO after thermal annealing is likely to be system-dependent and related to the molecular structure and thermal properties of the constituent components. Consequently, film drying dynamics during thermal annealing and the resultant film nanomorphology will also be system-dependent. In this study, we find that PBDB-T:ITIC-d₅₂ blend films have higher α values compared to analogous PBDB-T:PC₇₁BM films, prepared with the same DIO concentration, suggesting a higher degree of phase-separation. Given the similar Flory–Huggins interaction parameters estimated for PBDB-T with ITIC and PC₇₁BM,^[54] and their similar solubilities in DIO,^[25] we suspect this effect is primarily driven by differences in the drying dynamics.

For solvent-rich, as-cast films, the scattering exponent decreases with increasing DIO concentration for both fullerene and NFA systems due to higher amounts of residual DIO in the film. After thermal annealing, all PBDB-T:ITIC-d₅₂ films display an increase in α which is likely due to a combination of a higher degree of phase-separation and evaporation of DIO from the film. This is in agreement with results elsewhere which report increased vertical phase-segregation in PBDB-T:ITIC systems when processing with larger volume concentrations of DIO.^[34] Interestingly, PBDB-T:PC₇₁BM films processed without DIO demonstrate a decrease in α from 2.90 to 2.64 after thermal annealing, indicative of a lower degree of phase separation. This effect has been observed previously for P3HT:PC₆₁BM systems,^[51,55] and suggests drying behavior somewhat different to NFA systems, in that fullerenes, can more easily diffuse into PBDB-T domains due to their smaller molecular structure and larger diffusion coefficients.^[14,56] PBDB-T:PC₇₁BM films processed with DIO also have a higher α after annealing, indicative of domain coarsening, and this effect is greater when processed with larger DIO concentrations. After aging in ambient conditions for 1 year, all films exhibit slightly higher α values indicating ongoing domain coarsening over time. Albeit subtle, this effect shows that aging is taking place.

At smaller q ($0.01 \text{ \AA}^{-1} < q < 0.04 \text{ \AA}^{-1}$) a correlation peak is visible. At even smaller q ($q < 0.01 \text{ \AA}^{-1}$), PBDB-T:ITIC-d₅₂ blend films processed with 0.5% DIO show an increase in scattering intensity after thermal annealing suggesting the presence of an additional, larger characteristic length scale with $\alpha \approx 2.4$, (Figure S6, Supporting Information). We are unable to characterize this feature fully as it is beyond the observable q -range of the diffractometer used in this work.

2.2. Lorentz-Corrected Scattering Intensity

In Figure 3, we present the Lorentz-corrected SANS intensity (Iq^2 versus q) of all samples. This 1D representation displays the SANS data with no aberrations originating from the scattering geometry.^[57,58] The Lorentz correction should be used with caution and certainly, any data Lorentz corrected should not be fitted using standard scattering analysis software. In qualitative terms, the magnitude of the invariant, i.e., the integral under the Lorentz corrected SANS, gives information about the relative neutron SLD contrast in the system and hence the degree of phase separation/unmixing. In OPV blend films, the maximum in the invariant occurs when there are pure phases of the donor and acceptor components. A decrease in the invariant corresponds to a decrease in the SLD contrast within the system. This can arise

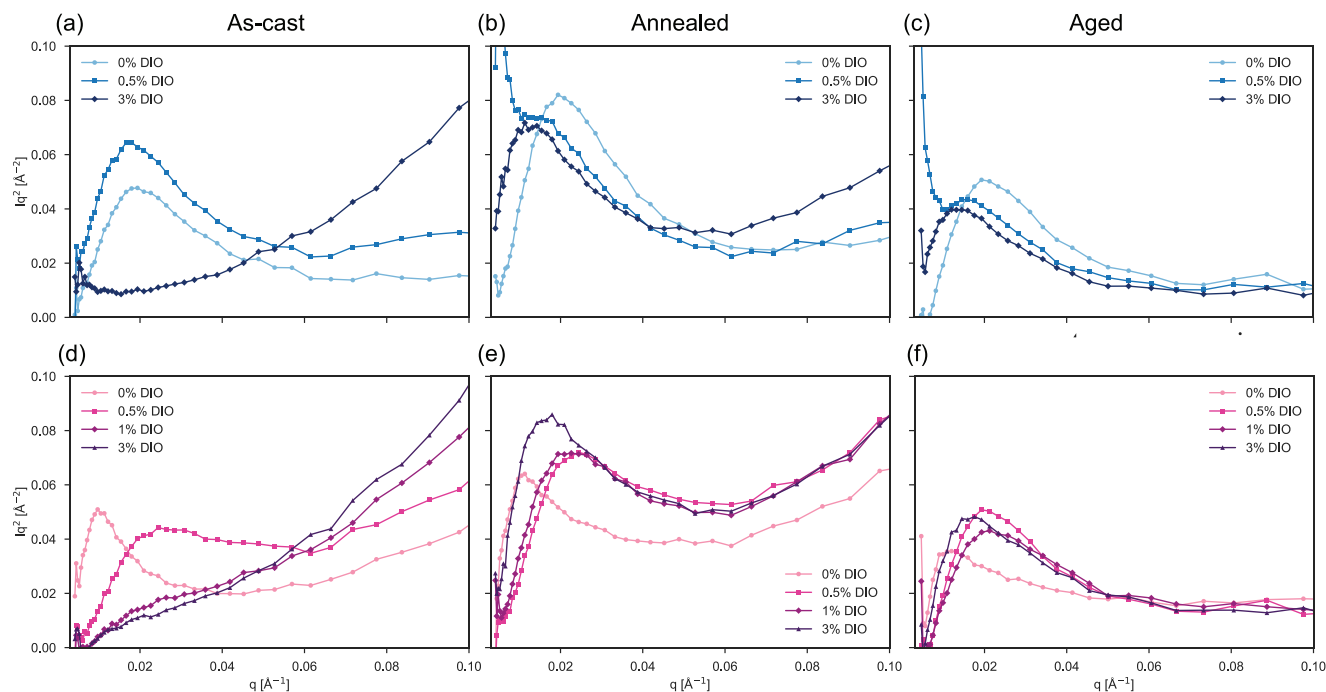


Figure 3. Lorentz-corrected SANS intensity (Iq^2 vs q) of as-cast, annealed and aged a–c) PBDB-T:ITIC- d_{52} and d–f) PBDB-T:PC $_{71}$ BM blend films processed with 0–3 vol% DIO.

due to various factors including the presence of leftover solvent in the film following processing, the crystallization of a particular component, or component mixing.^[59]

Due to the lower SLD of DIO compared to PBDB-T, PC $_{71}$ BM, and ITIC- d_{52} , ($\rho_{\text{DIO}} = 0.12 \times 10^{-6} \text{ \AA}^{-2}$), residual DIO will reduce the neutron SLD contrast in the blend and consequently the measured scattering intensity and invariant will be reduced. Additionally, the increased C:H ratio will contribute to a larger incoherent scattering background. These effects are most apparent in the as-cast blend films processed with 1 and 3 vol% DIO (Figure 3a,d). For all blend films processed with DIO, we observe an increase in scattering intensity after thermal annealing, which we suspect is due to the simultaneous removal of DIO and increase in SLD contrast between the polymer and acceptor (Figure 2b,e). This is also qualitatively evidenced by an increase in the Lorentz-corrected scattering intensity corresponding to a larger invariant signal (Figure 3e,f). The simplest case is for the scenario without DIO, where we see an increase in the invariant upon thermal annealing, followed by a reduction upon aging. If this is mirrored in the DIO systems, it can all be explained in terms of nanoparticle clustering due to phase separation and nanoparticle surface attraction, upon heating.^[60] With a very slow diffusion mechanism driving the NFA and fullerene into the thermally depleted polymer regions when the system is aged at ambient, i.e., below the polymer T_g .

In systems with periodic structures, a peak in the Lorentz-corrected SANS intensity (q_{peak}) represents the Bragg period L ($L = 2\pi/q_{\text{peak}}$).^[61] For OPV systems, L is often interpreted as the overall size of a domain of one phase.^[39,51,59] However, in such systems, there is also likely to be scattering contributions from structures other than the underlying periodic structure which may impact derived values. As-cast blend films processed with

1 and 3 vol% DIO do not display a peak in the Lorentz corrected scattering intensity due to retained DIO in the films and hence a lack of SLD contrast (Figure 3a,d). In comparison, films processed without DIO or with a low concentration of DIO (0.5 vol%) display a prominent peak in the Lorentz-corrected SANS intensity corresponding to a characteristic length scale L (summarized in Table 2). Comparing the inclusion of 0.5% DIO in the casting solution for as-cast films with films processed without DIO, we find differing behavior for PBDB-T:ITIC and PBDB-T:PC $_{71}$ BM systems. In the NFA system, L increases slightly from 34.7 to 37.2 nm but decreases significantly for the fullerene system from 64.8 to 25.8 nm, suggesting intercalation of the fullerene into the polymer.

Comparing thermally annealed films processed with DIO, we find that L increases for both blend systems but PBDB-T:PC $_{71}$ BM blend films processed with DIO generally demonstrate smaller L values compared with analogous NFA systems. After 1 year of aging under ambient conditions, L values for the PBDB-T:ITIC- d_{52} blend films decrease whilst L values for PBDB-T:PC $_{71}$ BM blend films increase. This suggests morphological changes will be less detrimental to PBDB-T:ITIC device performance compared to PBDB-T:PC $_{71}$ BM as the nanomorphology will never exceed the exciton diffusion length.

2.3. SANS Modeling

Further quantitative analysis of the SANS data provides more detailed insight into the size of domains and the interfacial characteristics between different phases within the blend films. We first fit the SANS curves using the Debye–Anderson–Brumberger (DAB) model (Figure 4).^[62,63] The DAB model is a development

Table 2. Bragg period L calculated from the correlation peaks in the Lorentz-corrected SANS intensity shown in Figure 3. Note: There are no visible scattering peaks for as-cast blend films processed with 1% or 3% DIO.

	PBDB-T:ITIC-d ₅₂ L [nm]			PBDB-T:PC ₇₁ BM L [nm]			
	0% DIO	0.5% DIO	3% DIO	0% DIO	0.5% DIO	1% DIO	3% DIO
As-cast	34.7 ± 0.5	37.2 ± 0.4	–	64.8 ± 1.5	25.8 ± 0.7	–	–
Annealed	32.9 ± 0.5	44.8 ± 1.7	47.6 ± 2.6	55.6 ± 2.0	25.7 ± 0.4	30.4 ± 0.6	35.0 ± 1.7
Aged	32.2 ± 0.5	40.3 ± 1.3	46.4 ± 1.2	53.0 ± 2.9	31.9 ± 0.5	31.7 ± 0.6	41.3 ± 1.7

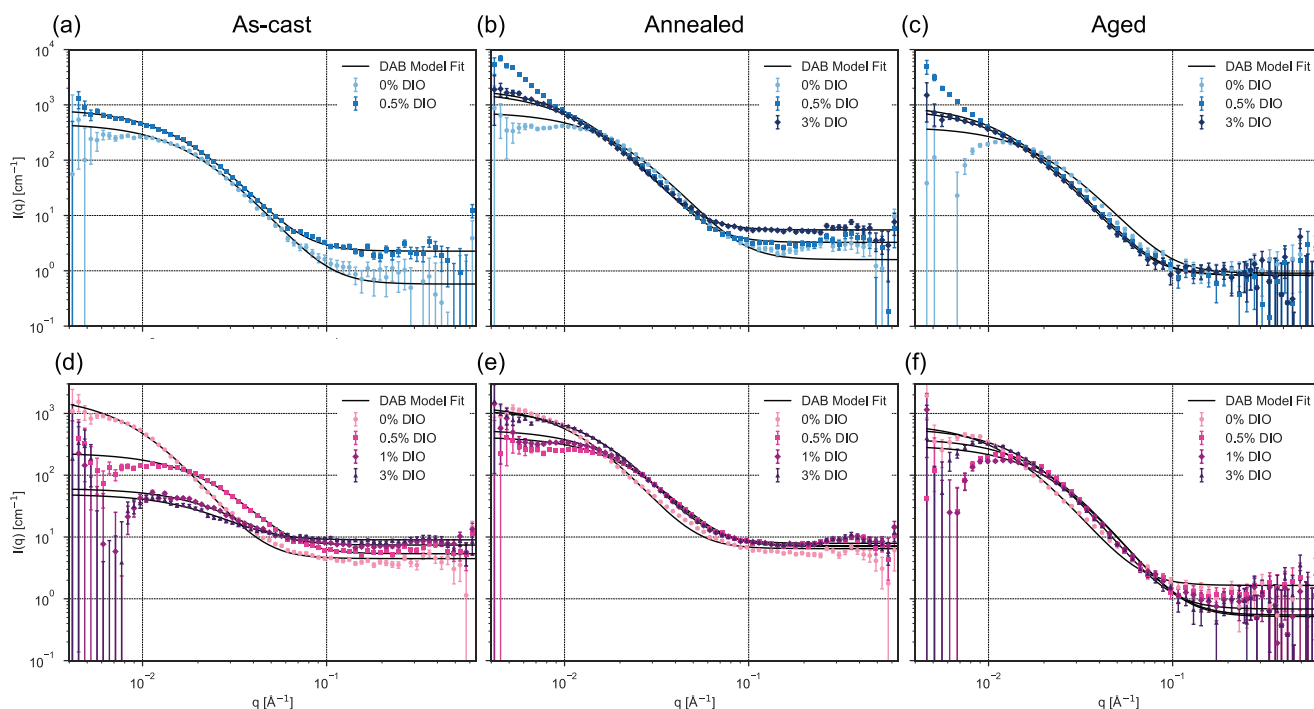


Figure 4. DAB model fits the SANS data for as-cast, annealed, and aged a–c) PBDB-T:ITIC-d₅₂ and d–f) PBDB-T:PC₇₁BM blend films processed with 0–3 vol% DIO. Note that 3% DIO PBDB-T:ITIC-d₅₂ as-cast fits were not fitted, as these systems were too solvated with DIO.

of the earlier Debye–Bueche model and is one of the simplest shape-independent models for characterizing a two-phase system.^[26,28,39,51,64] It calculates the scattering from a randomly distributed, two-phase system characterized by a single length scale, the correlation length ξ which is a measure of the average separation between domains of the same phase (see Supporting Information for further details).^[62,63,65]

In general, PBDB-T:ITIC-d₅₂ blend films processed with DIO exhibit a larger correlation length than PBDB-T:PC₇₁BM blend

films processed with the same concentration of DIO (Table 3). This agrees with the larger scattering exponents and Bragg period values discussed previously for NFA-based systems suggesting a more phase-separated system of larger domains compared to fullerene-based systems. After thermal annealing, all blend films processed with DIO show an increase in ξ in agreement with the increase in α discussed above. Comparing annealed and aged blend films, we note there are some subtle changes in ξ , decreasing by less than ≈ 0.5 nm for most systems. We presume

Table 3. Correlation lengths ξ obtained from Debye–Anderson–Brumberger (DAB) fitting the full observable q -range of the absolute scattering profiles shown in Figure 2 (full fit parameters provided in Table S3, Supporting Information).

	PBDB-T:ITIC-d ₅₂ ξ [nm]			PBDB-T:PC ₇₁ BM ξ [nm]			
	0% DIO	0.5% DIO	3% DIO	0% DIO	0.5% DIO	1% DIO	3% DIO
As-cast	5.08 ± 0.03	5.91 ± 0.02	–	10.26 ± 0.07	3.84 ± 0.02	3.23 ± 0.06	3.55 ± 0.10
Annealed	5.06 ± 0.02	7.99 ± 0.03	7.89 ± 0.03	7.62 ± 0.04	4.07 ± 0.02	4.57 ± 0.02	6.03 ± 0.02
Aged	4.73 ± 0.03	7.29 ± 0.06	7.25 ± 0.07	7.03 ± 0.07	4.66 ± 0.03	4.34 ± 0.04	5.62 ± 0.04

that this small reduction in ξ is driven by thermodynamics and diffusion of SMA over this extended period, with some reduction in the scattering invariant.

Finally, we fit the SANS data using the empirical Guinier–Porod model which takes into consideration both the size and dimensionality of the scattering entities (further model details, fits and fit parameters are provided in the Supporting Information, Figure S7 and Table S4, Supporting Information). We find that the same trends discussed above are reproduced. For example, the scattering exponent of blend films processed with DIO increases due to the removal of DIO and the coarsening of domains. Upon aging, we find that the scattering exponent generally increases due to phase separation as morphologies evolve to their thermodynamic equilibrium.

3. Conclusion

In conclusion, we have reported the synthesis of a deuterated NFA analog (ITIC- d_{52}) to allow SANS measurements of polymer: NFA blend films with poor intrinsic neutron contrast. Using established SANS protocols, we have compared the morphological evolution of fullerene and NFA-based OPV systems processed with DIO, measuring films in their as-cast state, after thermal annealing and following aging for 1 year under ambient conditions. We have shown that solvent additive processing affects the nanoscale structure and morphological stability of fullerene and NFA-based systems differently, demonstrating that the same optimization protocols used extensively for fullerenes are not easily translated to NFA systems. NFA-based systems are characterized by larger, coarser domains compared to equivalent fullerene-based systems. This is likely related to the stronger tendency of NFAs to undergo π – π -stacking and aggregation compared to fullerenes. For this reason, smaller concentrations of DIO are usually required to achieve optimal NFA-based performance. Furthermore, the appropriate DIO concentration for optimized performance can be chosen by selecting the amount that balances interfacial diffuseness with a length scale close to the exciton diffusion length. After long-term aging, we find that both NFA-based and fullerene-based systems demonstrate some level of thermodynamic-induced domain coarsening. However, for polymer: NFA blends we find that domain size (L) does not increase during morphological aging and as such is expected to possess good long-term operational device stability as the domain size will not exceed the exciton diffusion length. For polymer: fullerene blends, domain size generally increases during morphological aging indicating fullerene-based devices will possess inferior long-term operational stability. This work was made possible by the high sensitivity of SANS which is capable of probing subtle interfacial and domain size changes in the length scale range ≈ 1 –100 nm across an averaged bulk sample, provided there is sufficient neutron SLD contrast. We note that whilst this study has focused on blend materials optimized for PV applications, the results are also broadly applicable to a wide range of optoelectronic applications, which rely on solution-processed blend films.

4. Experimental Section

Materials: All solvents were purchased from Sigma–Aldrich. PEDOT: PSS (AI 4083), PC₇₁BM (95% purity), and PBDB-T ($M_w = 70\,532$, M1002)

were purchased from Ossila. Synthesis details and NMR characterization of the deuterated ITIC analog are provided in the Supporting Information (Note S2, Supporting Information: ITIC- d_{52} Synthesis and Characterization).

Sample Preparation: Samples were prepared via spin-coating with a quartz/PEDOT: PSS/active layer architecture. Each sample consisted of 15 stacked films prepared on PEDOT: PSS-coated quartz discs and secured in an aluminum sample holder. Quartz discs (Knight Optical, 15 mm diameter, 0.5 mm thick, WHQ15001-C) were cleaned by ultrasonication in a water bath held at ≈ 50 °C for 10 min in Hellmanex III (Ossila) diluted with deionized water (DI) (3: 1 DI water: Hellmanex III). The substrates were then rinsed extensively with DI water, sonicated for a further 10 min in DI water, and a final 10 min sonication in isopropyl alcohol. After drying with a nitrogen gun, the substrates were then treated for a further 15 min in a UV-ozone cleaner (Bioforce). PEDOT: PSS solution was stored in a refrigerator at 5 °C and filtered immediately before use, using a PVDF 0.45 μm microdisc filter. PEDOT: PSS films were prepared by spin-coating the filtered solution in ambient conditions at 6000 rpm for 30 s, producing films with a thickness of ≈ 40 nm. The samples were then transferred to a hotplate to thermally anneal the PEDOT: PSS film at 110 °C for 15 min under ambient conditions. PBDB-T: ITIC- d_{52} (1:1, w-w%) and PBDB-T: PC₇₁BM (1:1, w-w%) active layer solutions were prepared in chlorobenzene at a solid concentration of 18 mg mL⁻¹ (PBDB-T: ITIC- d_{52}) and 15 mg mL⁻¹ (PBDB-T: PC₇₁BM). Solutions were left stirring overnight at 60 °C for at least 12 h in a nitrogen-filled glovebox. The films were dynamically deposited via spin-coating in ambient conditions at 2000 rpm (PBDB-T: ITIC- d_{52}) and 1500 rpm (PBDB-T: PC₇₁BM) for 40 s to produce films with a thickness of ≈ 80 –120 nm. Thermal annealing was performed at 160 °C for 10 min in ambient conditions. The same samples were re-measured after storage in the dark under ambient conditions for ≈ 1 year.

Small Angle Neutron Scattering: SANS measurements were performed on the Larmor diffractometer at ISIS Pulsed Neutron and Muon Source. In SANS configuration, Larmor utilizes neutrons with a wavelength between 0.9 and 13.0 Å to probe a q -range of $0.003 \text{ \AA}^{-1} \leq q \leq 0.7 \text{ \AA}^{-1}$. Here q is the magnitude of the scattering vector equal to $q = 4\pi \sin\theta/\lambda$ where 2θ is the scattering angle and λ is the neutron wavelength. For all measurements, the beam diameter was collimated to 10 mm at the sample. All samples were measured for 240 μA (≈ 6 h). Each raw scattering data set was radially averaged and corrected for sample transmission, background scattering, detector efficiency, and sample thickness.^[66] Here, the sample thickness was taken as the total thickness of the blend films in the sample stack. To do this, the thickness of a few films from each sample stack was measured using Dektak profilometry (Bruker) and averaged. The background sample consisted of a stack of 15 PEDOT: PSS-coated quartz discs. For aged samples, an aged PEDOT: PSS sample stack aged under the same conditions as the blend film stacks was used. Corrected data was converted to scattering cross-sectional ($\partial\sigma/\partial\Omega$)(q) data, colloquially referred to as intensity $I(q)$, using Mantid software and plotted on an absolute scale (cm^{-1}).^[67] All data modelling was performed in SasView (version 5.0.5) using the Levenberg–Marquardt fit optimizer.^[68] Fits were evaluated using a goodness of fit chi-squared (χ^2) parameter normalized to the number of data points.

Atomic Force Microscopy: AFM measurements were performed on aged films using a Dimension 3100 (Veeco) microscope, equipped with a Nanoscope 3A feedback controller. Scout 350 RAI (NuNano) cantilevers were used with a resonant frequency of 350 kHz and spring constant of 42 N m⁻¹. The data was processed using Gwyddion software (Version 2.60).^[69] RMS roughness, mean roughness and power spectral density (PSD) values were extracted using the statistical quantities tool in Gwyddion.

Supporting Information

Supporting Information is available from the Wiley Online Library or from the author.

Acknowledgements

The authors acknowledge funding through the Engineering and Physical Sciences Research Council (UK) via grant EP/V055127/1. R.C.K. thanks the University of Sheffield for funding through a departmental teaching Ph.D. scholarship and the award of a publication scholarship. E.L.K.S. thanks the EPSRC for a Ph.D. studentship from the Centre for Doctoral Training in New and Sustainable PV, (EP/L01551X/1). A.C. thanks the Instituto de Telecomunicações (IT) for funding through Fundação para a Ciência e Tecnologia (FCT)/Portugal (contract no. UIDB/50008/2020). B.L.O. thanks for a research grant from IT under the project SUPRASOL (LISBOA-01-0145-FEDER-028365 – PTDC/QUI-QOR/28365/2017). G.B. thanks the Portuguese Foundation for Science and Technology (FCT) for his work contract (CEEC_IND/02039/2018) and the projects LA/P/0045/2020 (ALICE), UIDB/00511/2020 and UIDP/00511/2020 (LEPABE). The authors thank the ISIS Neutron and Muon Source for the award of beamtime on the Larmor diffractometer under experimental numbers RB1920285 and RB2010389. This work benefited from the use of the SasView application, originally developed under NSF award DMR-0520547. SasView contains code developed with funding from the European Union's Horizon 2020 Research and Innovation Program under the SINE2020 project, grant agreement no. 654000.

Conflict of Interest

D.G.L. is a co-director of the company Ossila Ltd. which retails materials and equipment used in organic photovoltaic device research and development.

Author Contributions

R.C.K. and E.L.K.S. designed the experiment and prepared blend film samples. R.C.K., E.L.K.S., S.L.B., and R.D. performed the SANS measurements. R.C.K. processed and analyzed the SANS data with assistance from A.J.P., R.D., and S.K. B.L.O., A.C. and G.B. synthesized the deuterated ITIC analog and performed NMR characterization. A.J.P., D.G.L. and R.A.L.J. supervised the study. All authors contributed to writing the manuscript.

Data Availability Statement

The data that support the findings of this study are openly available in ISIS database at 10.5286/ISIS.E.RB1920285, reference number 1920285.

Keywords

1,8-diiodooctane, nonfullerene acceptors, organic photovoltaics, small angle neutron scattering, solvent additives

Received: November 30, 2023

Revised: March 4, 2024

Published online:

- [1] K. Fukuda, K. Yu, T. Someya, *Adv. Energy Mater.* **2020**, *10*, 2000765.
 [2] R. Meitzner, U. S. Schubert, H. Hoppe, *Adv. Energy Mater.* **2021**, *11*, 1.
 [3] L. Zhu, M. Zhang, J. Xu, C. Li, J. Yan, G. Zhou, W. Zhong, T. Hao, J. Song, X. Xue, Z. Zhou, R. Zeng, H. Zhu, C. Chen, R. C. I. Mackenzie, Y. Zou, J. Nelson, Y. Zhang, Y. Sun, *Nat. Mater.* **2022**, *21*, 656.
 [4] Y. Lin, J. Wang, Z.-G. Zhang, H. Bai, Y. Li, D. Zhu, X. Zhan, *Adv. Mater.* **2015**, *27*, 1170.
 [5] W. Zhao, D. Qian, S. Zhang, S. Li, O. Inganäs, F. Gao, J. Hou, *Adv. Mater.* **2016**, *28*, 4734.
 [6] C. Lee, A. Yi, H. J. Kim, M. Nam, D.-H. Ko, *Adv. Energy Sustain. Res.* **2021**, *2*, 2100041.
 [7] A. Wadsworth, M. Moser, A. Marks, M. S. Little, N. Gasparini, C. J. Brabec, D. Baran, I. McCulloch, *Chem. Soc. Rev.* **2019**, *48*, 1596.
 [8] Z. Li, X. Li, Q. Yang, K. Ren, G. Nian, Z. Xie, *Org. Electron.* **2020**, *81*, 105690.
 [9] M. Riede, D. Spoltore, K. Leo, *Adv. Energy Mater.* **2021**, *11*, 2002653.
 [10] Y. Zhang, M. T. Sajjad, O. Blaszczyk, A. J. Parnell, A. Ruseckas, L. A. Serrano, G. Cooke, I. D. W. Samuel, *Chem. Mater.* **2019**, *31*, 6548.
 [11] Y. Firdaus, V. M. Le Corre, S. Karuthedath, W. Liu, A. Markina, W. Huang, S. Chattopadhyay, M. M. Nahid, M. I. Nugraha, Y. Lin, A. Seitkhan, A. Basu, W. Zhang, I. McCulloch, H. Ade, J. Labram, F. Laquai, D. Andrienko, L. J. A. Koster, T. D. Anthopoulos, *Nat. Commun.* **2020**, *11*, 1.
 [12] L. Ye, W. Zhao, S. Li, S. Mukherjee, J. H. Carpenter, O. Awartani, X. Jiao, J. Hou, H. Ade, *Adv. Energy Mater.* **2017**, *7*, 1602000.
 [13] M. Ghasemi, H. Hu, Z. Peng, J. J. Rech, I. Angunawala, J. H. Carpenter, S. J. Stuard, A. Wadsworth, I. McCulloch, W. You, H. Ade, *Joule* **2019**, *3*, 1328.
 [14] M. Ghasemi, N. Balar, Z. Peng, H. Hu, Y. Qin, T. Kim, J. J. Rech, M. Bidwell, W. Mask, I. McCulloch, W. You, A. Amassian, C. Risko, B. T. O'Connor, H. Ade, *Nat. Mater.* **2021**, *20*, 525.
 [15] Y. Qin, Y. Xu, Z. Peng, J. Hou, H. Ade, *Adv. Funct. Mater.* **2020**, *30*, 1.
 [16] G. Fang, J. Liu, Y. Fu, B. Meng, B. Zhang, Z. Xie, L. Wang, *Org. Electron. physics, Mater. Appl.* **2012**, *13*, 2733.
 [17] X. Yi, Z. Peng, B. Xu, D. Seyitliyev, C. H. Y. Ho, E. O. Danilov, T. Kim, J. R. Reynolds, A. Amassian, K. Gundogdu, H. Ade, F. So, *Adv. Energy Mater.* **2020**, *10*, 1902430.
 [18] C. McDowell, M. Abdelsamie, M. F. Toney, G. C. Bazan, *Adv. Mater.* **2018**, *30*, 1707114.
 [19] Y. Chen, X. Zhang, C. Zhan, J. Yao, *ACS Appl. Mater. Interfaces* **2015**, *7*, 6462.
 [20] L. Chang, H. W. A. Lademann, J. B. Bonekamp, K. Meerholz, A. J. Moulé, *Adv. Funct. Mater.* **2011**, *21*, 1779.
 [21] J. Peet, J. Y. Kim, N. E. Coates, W. L. Ma, D. Moses, A. J. Heeger, G. C. Bazan, *Nat. Mater.* **2007**, *6*, 497.
 [22] J. K. Lee, W. L. Ma, C. J. Brabec, J. Yuen, J. S. Moon, J. Y. Kim, K. Lee, G. C. Bazan, A. J. Heeger, *J. Am. Chem. Soc.* **2008**, *130*, 3619.
 [23] T. Salim, L. H. Wong, B. Bräuer, R. Kukreja, Y. L. Foo, Z. Bao, Y. M. Lam, *J. Mater. Chem.* **2011**, *21*, 242.
 [24] D. Sun, D. Meng, Y. Cai, B. Fan, Y. Li, W. Jiang, L. Huo, Y. Sun, Z. Wang, *J. Am. Chem. Soc.* **2015**, *137*, 11156.
 [25] X. Song, N. Gasparini, D. Baran, *Adv. Electron. Mater.* **2018**, *4*, 1700358.
 [26] G. Bernardo, H. Gaspar, G. E. Pérez, A. S. D. Shackelford, A. J. Parnell, M. Bleuél, A. Mendes, S. M. King, S. R. Parnell, *Polym. Test.* **2020**, *82*, 106305.
 [27] D. Yang, F. C. Löhner, V. Körstgens, A. Schreiber, S. Bernstorff, J. M. Buriak, P. Müller-Buschbaum, *ACS Energy Lett.* **2019**, *4*, 464.
 [28] Y. Zhang, A. J. Parnell, F. Pontecchiani, J. F. K. Cooper, R. L. Thompson, R. A. L. Jones, S. M. King, D. G. Lidzey, G. Bernardo, *Sci. Reports* **2017**, *7*, 1.
 [29] I. E. Jacobs, F. Wang, Z. I. Bedolla Valdez, A. N. Ayala Oviedo, D. J. Bilsky, A. J. Moulé, *J. Mater. Chem. C* **2018**, *6*, 219.
 [30] A. Classen, T. Heumueller, I. Wabra, J. Gerner, Y. He, L. Einsiedler, N. Li, G. J. Matt, A. Osvet, X. Du, A. Hirsch, C. J. Brabec, *Adv. Energy Mater.* **2019**, *9*, 1902124.
 [31] A. J. Pearson, P. E. Hopkinson, E. Couderc, K. Domanski, M. Abdjalebi, N. C. Greenham, *Org. Electron.* **2016**, *30*, 225.
 [32] W. Wang, F. Qin, X. Zhu, Y. Liu, X. Jiang, L. Sun, C. Xie, Y. Zhou, *ACS Appl. Mater. Interfaces* **2020**, *12*, 3800.

- [33] M. Kim, J. Lee, S. B. Jo, D. H. Sin, H. Ko, H. Lee, S. G. Lee, K. Cho, *J. Mater. Chem. A* **2016**, *4*, 15522.
- [34] L. M. Wang, L. M. Wang, Q. Li, S. Liu, Z. Cao, Y. P. Cai, X. Jiao, X. Jiao, H. Lai, W. Xie, X. Zhan, X. Zhan, T. Zhu, *ACS Appl. Mater. Interfaces* **2020**, *12*, 24165.
- [35] W. Chen, M. P. Nikiforov, S. B. Darling, *Energy Environ. Sci.* **2012**, *5*, 8045.
- [36] H. Gaspar, A. J. Parnell, G. E. Pérez, J. C. Viana, S. M. King, A. Mendes, L. Pereira, G. Bernardo, *Nanomaterials* **2021**, *11*, 3367.
- [37] Y. Gu, C. Wang, T. P. Russell, *Adv. Energy Mater.* **2012**, *2*, 683.
- [38] D. Chen, A. Nakahara, D. Wei, D. Nordlund, T. P. Russell, *Nano Lett.* **2011**, *11*, 561.
- [39] H. Chen, J. Chen, W. Yin, X. Yu, M. Shao, K. Xiao, K. Hong, D. L. Pickel, W. M. Kochemba, S. M. K. II, M. Dadmun, *J. Mater. Chem. A* **2013**, *1*, 5309.
- [40] H. Lu, B. Akgun, T. P. Russell, *Adv. Energy Mater.* **2011**, *1*, 870.
- [41] G. Bernardo, A. L. Washington, Y. Zhang, S. M. King, D. T. W. Toolan, M. P. Weir, A. D. F. Dunbar, J. R. Howse, R. Dattani, J. P. A. Fairclough, A. J. Parnell, *R Soc Open Sci* **2018**, *5*, 180937.
- [42] G. Bernardo, M. Melle-Franco, A. L. Washington, R. M. Dalgliesh, F. Li, A. Mendes, S. R. Parnell, *RSC Adv.* **2020**, *10*, 4512.
- [43] J. Kosco, M. Bidwell, H. Cha, T. Martin, C. T. Howells, M. Sachs, D. H. Anjum, S. G. Lopez, L. Zou, A. Wadsworth, W. Zhang, L. Zhang, J. Tellam, R. Sougrat, F. Laquai, D. M. DeLongchamp, J. R. Durrant, I. McCulloch, *Nat. Mater.* **2020**, *19*, 559.
- [44] C. M. Wolf, L. Guio, S. C. Scheiwiler, R. P. O'Hara, C. K. Luscombe, L. D. Pozzo, *Macromolecules* **2021**, *54*, 2960.
- [45] J. W. Kiel, A. P. R. Eberle, M. E. Mackay, *Phys. Rev. Lett.* **2010**, *105*, 168701.
- [46] T. P. Chaney, A. J. Levin, S. A. Schneider, M. F. Toney, *Mater. Horiz.* **2022**, *9*, 43.
- [47] D. Li, X. Chen, J. Cai, W. Li, M. Chen, Y. Mao, B. Du, J. A. Smith, R. C. Kilbride, M. E. O'Kane, X. Zhang, Y. Zhuang, P. Wang, H. Wang, D. Liu, R. A. L. Jones, D. G. Lidzey, T. Wang, *Sci China Chem* **2020**, *63*, 1461.
- [48] L. Zhang, F. Yang, X. Meng, S. Yang, L. Ke, C. Zhou, H. Yan, X. Hu, S. Zhang, W. Ma, Y. Yuan, *Org. Electron.* **2021**, *89*, 106027.
- [49] J. Mai, Y. Xiao, G. Zhou, J. Wang, J. Zhu, N. Zhao, X. Zhan, X. Lu, *Adv. Mater.* **2018**, *30*, 1802888.
- [50] Power_Law — SasView 5.0.5 Documentation, https://www.sasview.org/docs/user/models/power_law.html (accessed: November 2023).
- [51] W. Yin, M. Dadmun, *ACS Nano* **2011**, *5*, 4756.
- [52] L. Ye, S. Li, X. Liu, S. Zhang, M. Ghasemi, Y. Xiong, J. Hou, H. Ade, *Joule* **2019**, *3*, 443.
- [53] B. J. Tremolet De Villers, K. A. O'Hara, D. P. Ostrowski, P. H. Biddle, S. E. Shaheen, M. L. Chabinc, D. C. Olson, N. Kopidakis, *Chem. Mater.* **2016**, *28*, 876.
- [54] Q. Li, L. M. Wang, S. Liu, X. Zhan, T. Zhu, Z. Cao, H. Lai, J. Zhao, Y. Cai, W. Xie, F. Huang, *ACS Appl. Mater. Interfaces* **2019**, *11*, 45979.
- [55] N. D. Treat, M. A. Brady, G. Smith, M. F. Toney, E. J. Kramer, C. J. Hawker, M. L. Chabinc, *Adv. Energy Mater.* **2011**, *1*, 82.
- [56] N. D. Treat, T. E. Mates, C. J. Hawker, E. J. Kramer, M. L. Chabinc, *Macromolecules* **2013**, *46*, 1002.
- [57] O. Glatter, O. Kratky, *Small Angle X-Ray Scattering*, Academic Press, London; New York, **1982**.
- [58] O. Kratky, *Pure Appl. Chem.* **1966**, *12*, 483.
- [59] A. J. Parnell, A. J. Cadby, O. O. Mykhaylyk, A. D. F. Dunbar, P. E. Hopkinson, A. M. Donald, R. A. L. Jones, *Macromolecules* **2011**, *44*, 6503.
- [60] H. C. Wong, J. T. Cabral, *Phys. Rev. Lett.* **2010**, *105*, 38301.
- [61] G. R. Strobl, M. Schneider, *J. Polym. Sci., Polym. Phys. Ed.* **1980**, *18*, 1343.
- [62] P. Debye, H. R. Anderson, H. Brumberger, *J. Appl. Phys.* **2004**, *28*, 679.
- [63] Dab — SasView 5.0.5 documentation, <https://www.sasview.org/docs/user/models/dab.html> (accessed: November 2023).
- [64] H. Chen, Y.-C. Hsiao, B. Hu, M. Dadmun, *Adv. Funct. Mater.* **2014**, *24*, 5129.
- [65] P. Debye, A. M. Bueche, *J. Appl. Phys.* **2004**, *20*, 518.
- [66] SANS ISIS Data Reduction – Mantid Project, https://www.mantidproject.org/SANS_ISIS_Data_Reduction.html (accessed November 2023).
- [67] Mantid, <https://www.mantidproject.org/> (accessed: November 2023).
- [68] SasView – Small Angle Scattering Analysis, <https://www.sasview.org/> (accessed: November 2023).
- [69] D. Nečas, P. Klapetek, *Cent. Eur. J. Phys.* **2012**, *10*, 181.